

Optimal Design of the Bearingless Induction Motor for Industrial Applications

Jiahao Chen*, Eric L. Severson*

*Department of Electrical and Computer Engineering, University of Wisconsin-Madison, Madison, WI 53706 USA

Abstract—This paper presents a framework for the optimal design of the bearingless induction motor intended for industrial compressor applications. A pole-specific rotor winding and a combined stator winding are used to improve the machine performance. An initial design is constructed by following a standard design procedure for AC machines. Design considerations and motor performance evaluation that are unique to the bearingless induction motor are discussed. The 50 kW, 30,000 r/min bearingless induction motor is optimized using multi-objective evolutionary algorithm based on decomposition (MOEA/D). The Pareto front is shown in terms of torque density, efficiency, and ripple performance. Three optimal designs are selected according to different criteria. The improvement margin and tolerance of an optimal design is further investigated through a local sensitivity analysis. Typical optimized designs are found to have an efficiency of around 95.4% using 29-gauge M-19 steel and require less than 1% of the slot space for suspension current to levitate the rotor shaft.

Index Terms—high speed motor, multi-objective optimization, sensitivity, no voltage combined winding, pole-specific winding.

I. INTRODUCTION

Bearingless motors integrate the functionality of an active magnetic bearing (AMB) and an electric motor into a single electric machine. They have the potential to overcome several issues associated with motor systems that rely on distinct magnetic bearings. Historically, development efforts on bearingless motor technology have focused on lower power designs, often for niche applications such as left ventricle assist devices.

There have been several recent attempts to design medium and high power bearingless motors, for example [1]–[7]. In [1], a 24 slot, 4 pole, 30,000 rpm, 50 kW interior permanent magnet synchronous motor (IPMSM) is designed with stator skew to reduce torque ripple, and a 5 kW IPMSM prototype is built in [2] including an analysis of power factor. In [3], 6 slot, 4 pole, 30,000 rpm, 57 kW PMSMs in both interior and surface mounted configurations, are compared with different magnet pole angle and stator/rotor skew, and in order to ensure low force error angle, the magnet pole angle is found between 67° and 70°. In [5], after a comparison among different motor configurations, the authors suggest to use neodymium bonded PM instead of neodymium sintered PM to reduce the PM eddy current loss in the proposed 6 pole, 9 slot, 60,000 rpm, 25 kW SPMSM. In [4], an analytical optimization based pre-design is done prior to the finite element analysis (FEA) based optimization of the 5 kW, 30,000 rpm IPMSM, where

This work was supported by a scholarship from the China Scholarship Council (CSC) under Grant 201806320062 and by the Wisconsin Electric Machines and Power Electronics Consortium (WEMPEC).

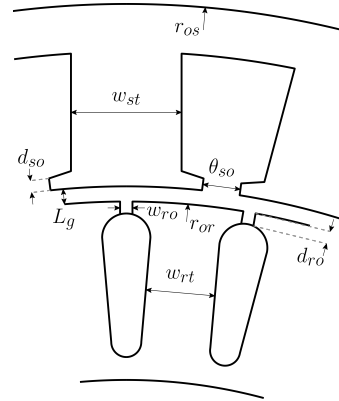


Fig. 1. Parameterization of bearingless IM geometry.

a reluctance network model is developed to capture motor force performance. In [6], 6 slot, 4 pole, 30,000 rpm, 50 kW bearingless PMSMs are optimized using a single objective optimization with a cost function constructed as a weighted sum of 6 objectives. In [7], the structural performance of the sleeved rotor is further taken into account into optimization. All of the high power designs mentioned above focus on bearingless PMSMs, and a single objective optimization approach is used for design optimization. However, within the broader field of machine design optimization, the Pareto non-dominated sorting based multi-objective optimization (MOO) is typically favored (see, e.g., [8]) and will be utilized in this paper.

Induction motors (IMs) have long been popular in industrial applications due to their low cost and high reliability and are also common for high speed designs due to their robust rotor structure [9]. The design of bearingless versions of IMs involves significantly design complexity but has received only very limited research attention [10]–[12]. Current literature on the bearingless IM has a focus on control [13]–[16] or sensing [17]–[19]. This paper, however, aims to develop an optimal design of a bearingless IM for industrial compressor applications of significant power levels. In a recent paper by the authors [12], computational efficient FEA modeling methods for bearingless IMs are proposed and discussed, which makes the optimization work in this paper possible.

To the authors' knowledge, this will be the first paper to present a detailed design optimization of a bearingless IM. The primary contributions of this paper are to: 1) develop an optimization framework for a bearingless IM, including a sensitivity analysis and a computationally efficient transient

Table I
GEOMETRIC VARIABLES, BOUNDS AND SELECTED OPTIMAL DESIGNS

Geometric Parameters	Symbols (x)	Symbols (x)	Bounds (\mathcal{B})	Initial (x_{ini})	High TRV	High η	Low Ripple (x_{optm})
Air gap length	L_g [mm]	x_1	[1.1, 2.5]	1.27	1.15	1.26	1.39
Stator tooth width	w_{st} [mm]	x_2	[4.0, 12]	7.97	8.97	6.80	8.68
Rotor tooth width	w_{rt} [mm]	x_3	[2.8, 8.4]	5.58	8.34	5.64	7.97
Stator slot opening angle	θ_{so} [deg]	x_4	[1.5, 12]	3.00	3.23	5.85	2.83
Rotor slot opening width	w_{ro} [mm]	x_5	[0.5, 3.0]	0.94	0.76	1.59	0.59
Stator slot opening depth	d_{so} [mm]	x_6	[0.5, 3.0]	1.00	2.82	2.12	1.98
Rotor slot opening depth	d_{ro} [mm]	x_7	[0.5, 3.0]	1.00	1.12	2.58	1.46

FEA technique; and 2) present a MOO of a bearingless IM design for medium to high power industrial compressors. The bearingless IM considered in this paper provides 2 degrees-of-freedom for shaft suspension. To form a fully levitated system, a combined radial axial AMB can be further used, as described in [20].

II. BEARINGLESS IM CONFIGURATION FROM A HIGH SPEED IM PERSPECTIVE

The design of a high speed IM and a bearingless IM share some common considerations from the aspect of high speed operation. For example, in order to avoid excessive iron loss, a larger air gap length is usually adopted [9], [21]. It is reported in [22] that the rotor iron loss can be mitigated by using an optimal slit length, using magnetic wedge, or adding notches to the stator teeth.

Three main design differences between high speed IM and bearingless IM can be summarized as follows. First, high speed IMs use contact bearings [23] or AMBs [24]–[26], while bearingless IMs integrate the functionality of AMB. Second, high speed IMs can use slit solid rotors, coated solid rotors, or cage rotors [24], [27]; for a bearingless motor, however, those rotor structures will experience undesired rotor currents induced by the suspension field. The authors have found that a typical bearingless IM with a cage rotor will consume 20% of rated current to merely lift the rotor weight at 500 Hz excitation (and this increases with frequency) [12]. Therefore, this paper considers a pole-specific rotor winding that is proposed exclusively for bearingless IM [28]. Lastly, the bearingless motor requires an extra stator suspension winding. In this paper, we consider a single combined winding, based on the technique described in [29].

III. BEARINGLESS IM MODELING

Fig. 1 shows the motor geometry parameterization used for this paper. Seven geometric variables are used to fully define a bearingless IM design; other geometric variables are either derived or specified. In other words, each design is determined by a vector $x \in \mathcal{B} \subset \mathbb{R}^7$:

$$x = [L_g \ w_{st} \ w_{rt} \ \theta_{so} \ w_{ro} \ d_{so} \ d_{ro}]^T \quad (1)$$

where \mathcal{B} denotes design space and is presented in Table I.

A. The Initial Template Design

The design specifications of the bearingless IM are 50 kW and 30,000 rpm. Based on an analytical design procedure [12],

[30], an initial design $x_{\text{ini}} \in \mathcal{B}$ is first established, as shown in Table I. The initial design has $Q_s = 24$ and $Q_r = 32$ slots for the stator and rotor, respectively and has $p = 2$ pole pair torque winding and $p_s = 1$ pole pair suspension winding. The stator outer diameter and rotor inner diameter of this initial design are respectively $D_{os} = 184$ mm and $D_{ir} = 31.6$ mm. This initial design will be used as a template during the optimization in the sense that all individuals that are “born” during evolutionary optimization are variants of this template with a different vector of x . For example, the stator and rotor yoke depths of the new-born individuals retain the template design values of D_{os} and D_{ir} .

B. Tip Speed and Rotor Outer Radius

Based on the high speed IM design examples from the literature (see, e.g., [27], [30]), the tip speed of a laminated rotor should be below below 200 m/s. As a result, the tip speed is specified as 150 m/s in this paper. The tip speed determines the rotor outer radius $r_{or} = 47.7$ mm in this paper. The stress on lamination due to centrifugal loading can be calculated by analytic equations (see e.g., [31]) or structural FEA, and it has to be below the yield stress of the lamination material up to a safety factor usually between 1.5 and 2.

C. Current Density and Slot Height

It is reported in the literature that the current density of rotor bars in high speed IMs can be up to 20 Arms/mm² [27], which surely demands the incorporation of forced cooling system. On the other hand, the typical rotor current density for general purpose IM is between 3 and 8 Arms/mm² [30]. In this paper, the rotor current density is assumed to be $J_r = 6.5$ Arms/mm². Note that the actual rotor current density may deviate from the this assumption if the actual power factor is different from the assumed one. The stator current density is fixed at $J_s = 4$ Arms/mm² and a stator slot fill factor of 0.5 is assumed.

The stator and rotor current values of the template design are used along with the current densities to determine the required slot area. The calculated slot area is combined with the tooth width to determine the necessary slot height for each design.

D. Rotor Winding Selection

The pole-specific rotor winding [28] is adopted in this paper to prevent rotor current from being induced by the suspension field. In our case, the pole-specific rotor winding is a 4 pole, 8 phase, full pitch wave winding shown in Fig. 2b. As a comparison, a cage rotor will result in low efficiency [32]

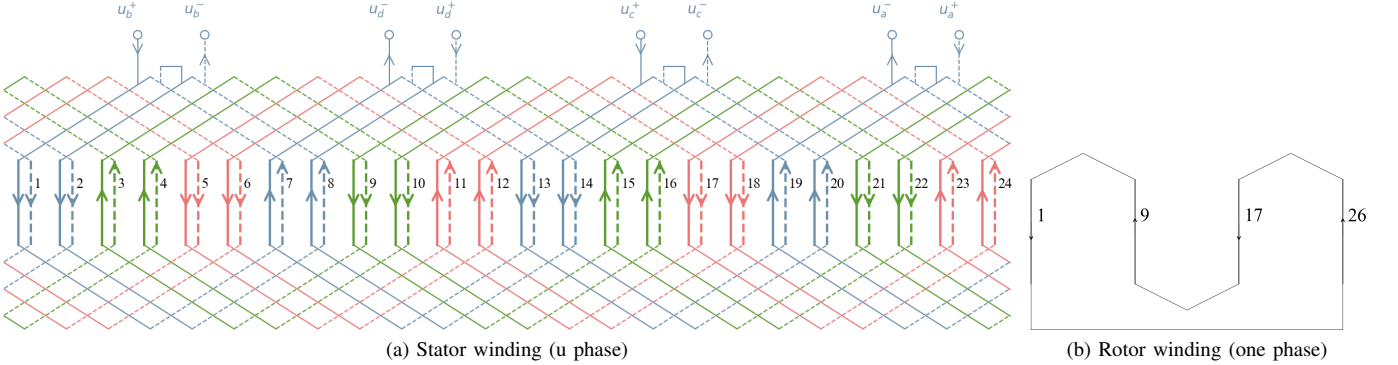


Fig. 2. Stator no voltage combined winding ($Q_s = 24$, $p = 2$, $p_s = 1$, $m = 3$) and rotor pole-specific winding ($Q_r = 32$, $p = 2$, $m = 8$), where m denotes number of phases.

with poor suspension force performance [12]. Finally, note that manufacturing this pole-specific rotor is challenging and will be considered in a future work.

E. Stator Winding Selection

The stator winding is implemented as a no voltage combined winding [33], shown in Fig. 2a. It has the feature of suspension inverter not being exposed to motor back electromotive force. As compared to separated winding, no slot space is permanently occupied for generating suspension field, which enables the design to have a higher efficiency and torque density.

In our case ($Q_s = 24$, $p = 2$, $p_s = 1$), the winding factor (i.e., distribution factor) of the suspension winding is relatively low (= 0.496) [29], because half of the stator MMF simply cancels each other out to build a $p_s = 1$ pole pair field. Note that having a low suspension winding factor is more acceptable than having a low torque winding factor. This is because the suspension winding rarely (if ever) needs to use its current rating to create large forces, while the torque winding is consistently operated at rated current.

Selecting the motor and suspension pole combination is a trade-off between motor and suspension performance. From the induction motor perspective, a $p = 2$ design is preferred as it yields a higher torque density while still obtaining an acceptable power factor [30]. Since $p_s = 3$ results in an invalid three phase no voltage winding [29], only the $p_s = 1$ design is possible. Note, however, that $p_s = p - 1$ designs have a reduced suspension force capability because the Lorentz and Maxwell forces are in opposing directions [34].

F. Selection of Iron Core Material

To select a proper steel material for high speed motors, three aspects should be considered according to motor rating and application. They are mechanical strength, magnetic performance, and cost.

First, it is reported in [35] that M-19 steel is not mechanically strong enough for the 2 MW, 15,000 rpm high speed IM with a tip speed of 286 m/s. Since the tip speed is only 150 m/s in this paper, the M-19 steel is still a feasible option. Second, it is usually suggested to use a thin lamination sheet (≤ 0.2 mm) to reduce the eddy current loss for high frequency motors

[9]. For example, the thickness of Arnon 5 steel is 0.127 mm. However, using thin lamination sheets is expensive and creates manufacturing challenges.

The 29-gauge (i.e., 0.355 mm thick) M-19 steel is adopted in this paper, which features low hysteresis losses and high saturation flux density compared with Arnon 5 steel. A fitting to Steinmetz equation using 29-gauge M-19 steel's loss data gives

$$C_e = 0.530 \frac{W}{m^3 T^2 Hz^2} \\ C_h = 143 \frac{W}{m^3 T^2 Hz} \quad (2)$$

where C_e and C_h are the coefficient for eddy current loss and hysteresis loss, respectively.

G. Motor Performance Evaluation Process

A two stage FEA simulation is implemented to evaluate the performance of a bearingless IM design. In stage one, the breakdown slip frequency that corresponds to the motor's maximum torque is first determined using eddy current FEA. To expedite the searching process, five instances of eddy current FEA at different slip frequencies are executed in parallel using FEMM [36].

In stage two, transient FEA is performed at the breakdown slip frequency using JMAG. In order to create suspension force, the stator excitation must be properly configured. In this paper, 97.5% of rated current is allocated for motor operation while the remaining 2.5% is allocated for producing suspension field. Based on the results of transient FEA, the fitness or the cost function of the design is calculated.

One major obstacle is that transient FEA is extremely time-consuming. To circumvent this issue, the authors have proposed and compared different FEA modeling techniques in [12]. The “transient FEA with two time step sections” is used in this paper, as it greatly reduces the simulation time of a (current source) transient FEA and exhibits the best accuracy in predicting suspension force performance over other computational efficient methods (i.e., rotor-rotating static FEA and eddy current FEA).

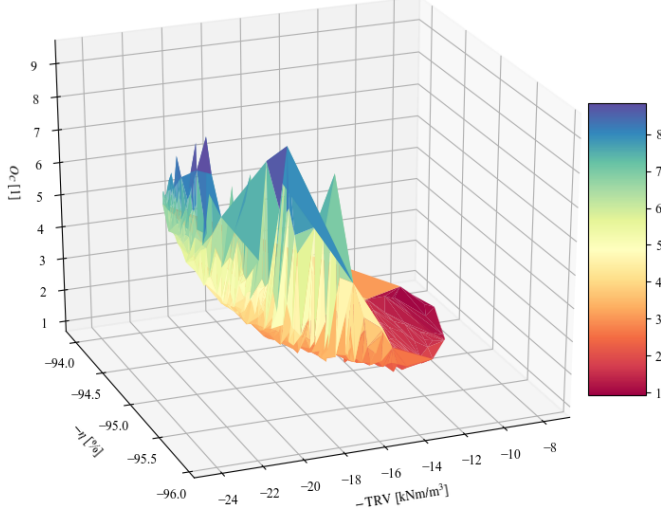


Fig. 3. The estimated 3D Pareto front based on all the evaluated designs. A triangulation technique is used to generate a surface among local points. The color of the triangular surface/segment indicates the average value of O_C of the local points.

IV. OPTIMIZATION PROBLEM DEFINITION

A. Optimization Problem

Bearingless IM optimization can involve multiple objectives. The ones used in this paper are torque per rotor volume (denoted by TRV [Nm/m^3]), force per rotor weight (FRW [p.u.]), normalized peak-to-peak torque ripple ($T_{\text{rip}} [\%]$), normalized force error magnitude ($E_m [\%]$), force error angle ($E_a [\text{deg}]$), and loss power ($P_{\text{loss}} [\text{W}]$).

For dealing with multiple objectives, two approaches are introduced in the following [8], [37].

1) *Weighted Sum Function of Multiple Objectives:* This approach is commonly used in optimization of bearingless motors. Recall the definition of geometric vector x in (1). The weighted sum objective function $O_j(x)$, $j = 1, 2$ is defined as [6]

$$O_j(x) = \left[\frac{30e3 \frac{\text{Nm}}{\text{m}^3}}{\text{TRV}} \quad \frac{T_{\text{rip}}}{5\%} \quad \frac{1}{\text{FRW}} \quad \frac{E_m}{5\%} \quad \frac{E_a}{1 \text{ deg}} \quad \frac{P_{\text{loss}}}{2500 \text{ W}} \right] w_j$$

$$w_1 = [1 \quad 0.1 \quad 1 \quad 0.1 \quad 0.1 \quad 0]^T$$

$$w_2 = [1 \quad 1 \quad 1 \quad 1 \quad 1 \quad 0]^T \quad (3)$$

in which, weight w_2 emphasizes more on the ripple performance than w_1 . During the comparison stage of this approach, design x_A survives over another design x_B if $O_j(x_A) < O_j(x_B)$ holds. As a result, the searching process highly depends on the weights selected. The local sensitivity analysis that will be mentioned later can also be used to examine whether or not a weight is good for a reference design.

2) *Pareto Non-dominated Sorting Method:* This approach is favored within the broader electric machines community to overcome shortcomings in the weighted function approach and will be the focus of this paper. The key concept of Pareto non-dominated sorting is Pareto dominance. We say that design x_A dominates another design x_B if all objective values of x_A are no worse than that of x_B and at least one of the objective

values of x_A is better than that of x_B . In this paper, three objectives are defined as follows

$$\begin{aligned} O_A &= -\text{TRV} \\ O_B &= -\eta \\ O_C &= T_{\text{rip}}/(5\%) + E_m/(5\%) + E_a/(1 \text{ deg}) \end{aligned} \quad (4)$$

in which, η is efficiency, and O_C is a weighted sum of ripple performance metrics. During the comparison stage of non-dominated sorting, the j -th new-born trial design $x_{j,\text{trial}}$ will be discarded if $x_{j,\text{trial}}$ does not dominate the j -th design x_j from the population. In order to rule out possible designs that have poor ripple performance but good TRV or η , three constraints are further imposed during optimization:

$$\begin{aligned} T_{\text{rip}} &< 20\% \\ E_m &< 20\% \\ E_a &< 10 \text{ deg} \end{aligned} \quad (5)$$

V. OPTIMIZATION PROCESS AND RESULTS

A. Optimization Algorithm

There are two popular MOO algorithms available, i.e., multi-objective evolutionary algorithm based on decomposition (MOEA/D) and non-dominated sorting genetic algorithm II (NSGA-II). It is reported in [38] that MOEA/D outperforms NSGA-II. Furthermore, MOEA/D works well with large population size while the convergence rate of NSGA-II is slowed with large population size [39]. Finally, the original MOEA/D is built for MOO problem of up to 4 objectives, which is suited for our case.

This paper adopts the differential evolution variant of MOEA/D implemented by the software PAGMO [40].

B. Results of MOO with MOEA/D

1) *Pareto Front Plot:* In the case of three objectives (O_A , O_B , O_C), the Pareto front is a surface in a 3D space. The actual Pareto front is never known, but in [8], a direct search (i.e., a design space sweeping) is applied to obtain a reference for the Pareto front. This, however, is not realistic to do for the bearingless IM design optimization. For example, a direct search with 7 steps for each design variable will result in $7^7 = 823,543$ designs, which translates into about 4.7 years to finish on a single PC. In this paper, an estimate of the Pareto front can be sketched using the archive (i.e., all the evaluated designs), as shown in Fig. 3.

In order to see clearly the performance of those designs on the estimated Pareto front, the points on the estimated Pareto front are projected to the O_B - O_A plane, i.e., $-\eta$ vs. $-\text{TRV}$ plane, as shown in Fig. 4a. In Fig. 4a, some points have worse torque density and efficiency but low O_C value such that they are not dominated by others and as a result, those points are still present on this 2D plot. The color of the scatter point shows the value of O_C . Generally speaking, a value of O_C below 3 means a design with low ripple performance. For example, $O_C = 3$ could mean $T_{\text{rip}} = 5\%$, $E_m = 5\%$, $E_a = 1 \text{ deg}$, and it implies that $E_a < 3 \text{ deg}$. Having a low E_a value is important for the bearingless motor to be stably levitated.

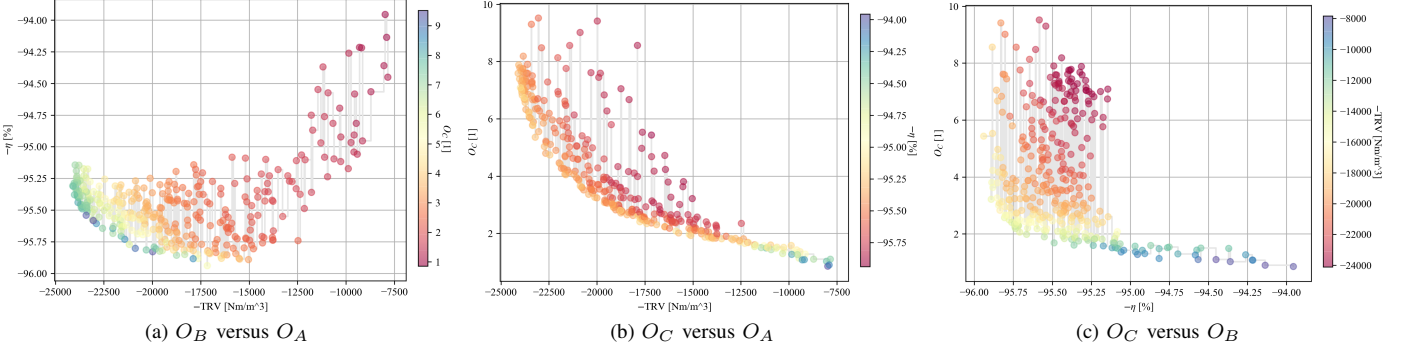
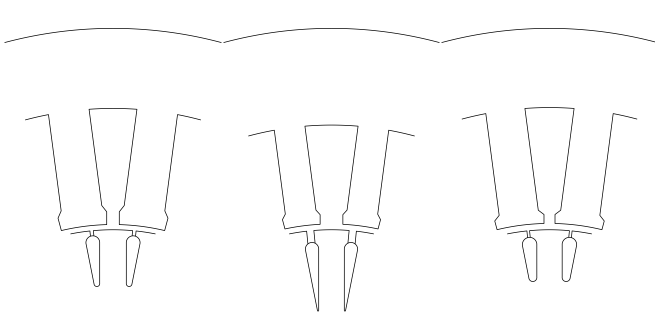


Fig. 4. The estimated 3D Pareto front projected to different 2D planes. Only the first rank Pareto front individuals are plotted.

Table II
SELECTED OPTIMAL DESIGNS AT RATED POWER

Design Name	Selection Criteria	TRV [Nm/m ³]	η	O_C	FRW [p.u.]
High torque density	$O_C < 5$, $O_B < -0.95$, $O_A < -22500$	22668.7	95.381%	4.796	4.0
High efficiency	$O_C < 10$, $O_B < -0.9585$, $O_A < -17500$	17633.3	95.885%	5.531	2.1
Low ripple	$O_C < 3$, $O_B < -0.95$, $O_A < -19000$	19169.0	95.423%	2.999	2.7
Design Name	T_{rip}	E_m	E_a	Breakdown slip frequency	Power factor
High torque density	16.6%	2.71%	0.94 deg	2.33 Hz	0.622
High efficiency	20.6%	1.73%	1.07 deg	2.75 Hz	0.638
Low ripple	11.5%	0.94%	0.51 deg	2.50 Hz	0.586
				Rotor weight	



(a) High TRV design (b) High η design (c) Low ripple design

Fig. 5. Cross-sectional view of the selected optimal designs.

2) *Conflicting Nature Among Objectives*: From the 2D Pareto front of O_B vs. O_A in Fig. 4a, one realizes that for the same torque density (e.g., 20,000 Nm/m³), efficiency can be traded with the ripple performance to a certain extent. This means a design with high torque density and high efficiency can be pursued if ripple performance is not a concern, since torque density and efficiency are weak conflicting objectives.

On the other hand, the 2D Pareto front of O_C vs. O_A in Fig. 4b shows ripple performance is conflicting with torque density. This means a design with low ripple performance and high torque density is not possible, since ripple performance and torque density are strong conflicting objectives.

In Fig. 4c, the Pareto front shows that the O_C and TRV can be traded with each other. Again, this implies there is a strong conflicting relation between ripple performance and torque density. On the other hand, ripple performance and efficiency are weak conflicting objectives and therefore, a low

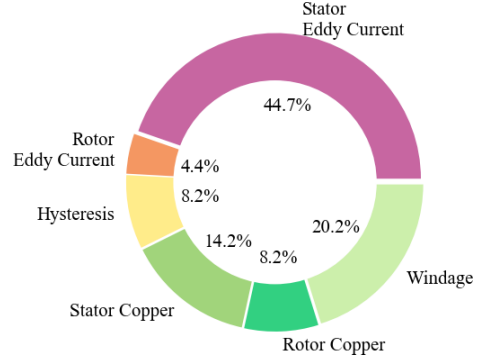


Fig. 6. The loss component breakdown of the low ripple design at rated power. The stator and rotor hysteresis losses are 8.1% and 0.1% of the total loss, respectively.

ripple, high efficiency design can be reached to a certain extent if torque density is not a concern.

An example is given here to provide more intuitive understanding of the strong and weak conflicting relations among objectives. For example, by specifying selection criterion of $O_C < 5$, the best TRV value is as high as 22669 Nm/m³ with $O_C = 4.80$ while the efficiency is around 95.38%. If, however, the selection criterion is $O_C < 3$, the best TRV value is reduced to 19169 Nm/m³ with $O_C = 3.00$ while the efficiency is around 95.42%. In other words, TRV is traded with O_C while η is nearly identical.

VI. SELECTED OPTIMAL DESIGNS AND SENSITIVITY ANALYSIS

A. Selection Criteria

Several optimal designs are selected by different criteria and have been summarized in Table II. Their values of geometric

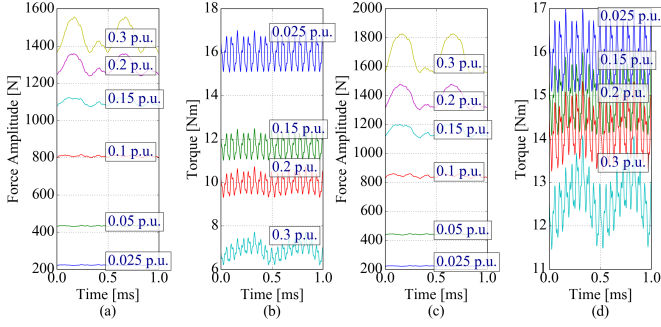


Fig. 7. Profiles of force amplitude and torque over one stator period. The boxed text shows the per unit value of suspension current. a), b) Rated current case. c), d) Over current case.

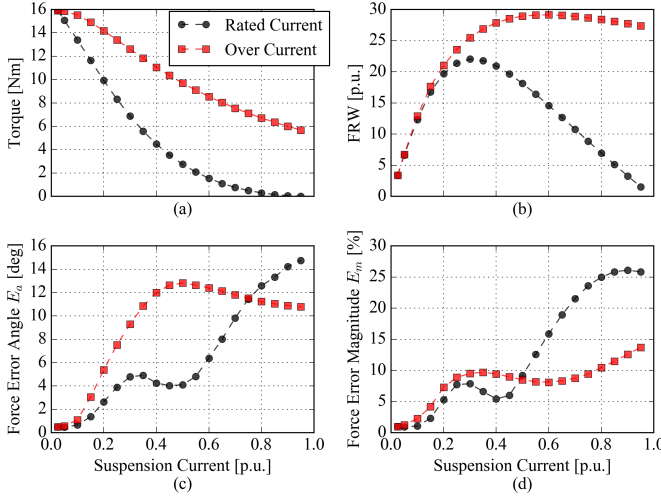


Fig. 8. Torque, FRW, E_a and E_m as a function of per unit value of suspension current. The base value for the suspension current and FRW are rated current and rotor weight, respectively. The motor slip is fixed at the breakdown slip.

variables are listed in Table I, and their cross-sectional sketches are shown in Fig. 5.

From Table II, the high torque density design has a TRV value of 22669 Nm/m³ which is in the range of high performance servomotors [41]. It also has an FRW value of 4.0 p.u., which means that it is able to support four times its rotor weight by using only 2.5% of the slot space for suspension current. Even though the high TRV design has a relatively high O_C value of 4.796, it does not necessarily have poor suspension force performance. In fact, the high TRV design has high torque ripple (16.6%) but low force ripple performance: $E_a = 0.94$ deg and $E_m = 2.71\%$. High torque ripple is expected because neither skew, short pitch stator winding, nor low ripple slot combination (e.g., $Q_s = 24$ and $Q_r = 30$) are used. This design may be optimal for some applications that are not sensitive to torque ripple performance.

By looking at Fig. 5, one realizes that the rotor slot height is actually dependent on both rotor tooth width w_{rt} and rotor slot opening depth d_{ro} . The low ripple design has the shortest rotor slot height, because according to Table I, it has smaller rotor tooth width w_{rt} than that of high TRV design, and it

has smaller rotor slot opening depth d_{ro} than that of the high η design.

B. Characteristics of the Bearingless IM Design

The detailed performance of the low ripple design is investigated as an example. The loss composition at rated power is shown in Fig. 6. The main loss component (44.7%) is the eddy current loss in the stator iron core, which means this design can have an improved efficiency if a thinner lamination material is used.

In order to show the suspension force capability of a bearingless motor, more transient FEA studies are performed for the low ripple design with different suspension current and torque current combinations, as shown in Fig. 7 and Fig. 8. The per unit (p.u.) is used to describe the suspension current with the base value equal to the rated current value (i.e., 1 p.u. means rated current). Two cases are considered: 1) “Rated Current” where the total current is fixed at the machine’s rated current, and 2) “Over Current” where the torque current is fixed at 97.5% of rated current and the suspension current is increased so that the winding is in an over current condition.

In Fig. 7, steady state profiles of the force amplitude and torque are drawn. For both cases, as the suspension current increases up to 0.3 p.u., the force amplitude increases while torque is reduced. Large force ripple is observed when the suspension current is beyond 0.15 p.u.

In order to describe the force ripple performance of a bearingless motor, force error angle E_a and force error magnitude E_m are introduced. E_a and E_m are defined as the angle and the magnitude difference between the desired force vector and the most deviated force vector over one stator period [12]. It is mentioned in literature that E_a being less than 5 deg does not cause significant negative effect on levitation control [3], [42]. Nonetheless, E_a being too large possibly results in the control system becoming unstable (e.g., 17 deg [42]).

Fig. 8 shows how the performance metrics (including E_a and E_m) vary with different combinations of torque current and suspension current. For the “Over Current” case, the force amplitude curve has a saturation-like behavior. When operating at maximal force amplitude, even though E_m is below 10%, E_a is over 12 deg. As for the “Rated Current” case, one observes that when suspension current is near 0.35 p.u., the bearingless motor’s force rating reaches 22 times the rotor’s weight (FRW = 22 p.u.) and corresponds to a ripple performance of $E_m = 7.9\%$ deg and $E_a = 4.9$ deg. This demonstrates the machine’s ability to create very large forces when needed.

C. Local Sensitivity Analysis

A local sensitivity analysis is now presented for the low ripple design (denoted as x_{optm}). This analysis is done to show the potential for further improvements to the design and to evaluate the design’s “robustness” for manufacturing.

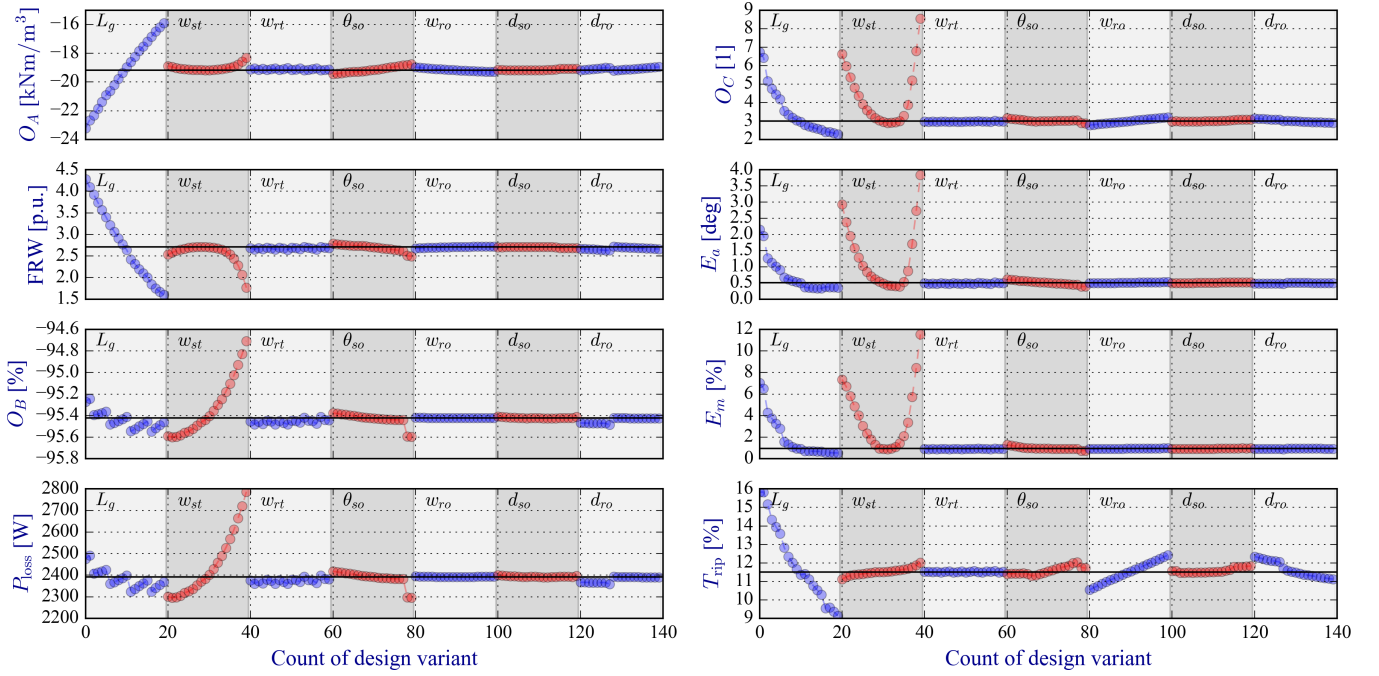


Fig. 9. Results of local sensitivity analysis for the optimal low ripple design x_{optm} . The 7 shaded regions correspond to 7 geometric variables x_i , $i = 1, 2, \dots, 7$. In each shaded region, the perturbation Δx_i changes evenly from $-20\%x_{\text{opti},i}$ to $20\%x_{\text{opti},i}$ in 20 steps. The black solid horizontal line indicates the performance of the selected optimal design x_{optm} .

To determine the design objectives' sensitivity with respect to the geometric variables x_i , $i = 1, 2, \dots, 7$, a perturbation Δx is added to x_{optm} , where Δx can be any of the following

$$\begin{aligned} \Delta x &= [\Delta L_g \ 0 \ 0 \ 0 \ 0 \ 0 \ 0]^T \quad \text{s.t. } x_{\text{optm}} + \Delta x \in \mathcal{B}_{\text{loc}} \\ \Delta x &= [0 \ \Delta w_{st} \ 0 \ 0 \ 0 \ 0 \ 0]^T \quad \text{s.t. } x_{\text{optm}} + \Delta x \in \mathcal{B}_{\text{loc}} \\ &\dots \\ \Delta x &= [0 \ 0 \ 0 \ 0 \ 0 \ 0 \ \Delta d_{ro}]^T \quad \text{s.t. } x_{\text{optm}} + \Delta x \in \mathcal{B}_{\text{loc}} \end{aligned}$$

where $\mathcal{B}_{\text{loc}} \subset \mathcal{B} \subset \mathbb{R}^7$ is a local neighborhood. In this paper, we vary each one of ΔL_g , Δw_{st} , Δw_{rt} , $\Delta \theta_{so}$, Δw_{ro} , Δd_{so} and Δd_{ro} to obtain 20 design variants from optimal design x_{optm} , i.e., 20×7 design variants in total.

The results of local sensitivity analysis for 140 design variants from x_{optm} are shown in Fig. 9, and are interpreted as follows.

- 1) If for a single design variant, O_A , O_B , O_C can be improved at the same time, a dominate design is found. In Fig. 9, one observes that very limited improvement can be done to x_{optm} .
- 2) The potential for improving the optimal design in terms of individual performance metrics is depicted. For instance, if the designer wants the low ripple design to have at least a TRV value of $20,000 \text{ Nm/m}^3$, according to Fig. 9, by reducing only air gap length L_g , this requirement can be satisfied with a worse $O_C = 3.4$ but an improved $\eta = 95.47\%$.
- 3) The robustness or tolerance of a design (see, e.g., [43]). Owing to error during manufacturing, some geometric variables are not exactly as expected. A robust or tolerant

design should have “flat” response in the partial derivative of performance metrics with respect to geometric variables. From Fig. 9, clearly, the robustness of the design is the worst for variation in L_g , w_{st} and w_{rt} .

- 4) In Fig. 9, most objectives are not sensitive to θ_{so} , w_{ro} , d_{so} and d_{ro} , except for torque ripple T_{rip} . This implies that L_g , w_{st} and w_{rt} are the critical parameters during optimization.

VII. CONCLUSION

This paper presents a work-flow for MOO of bearingless IMs using MOEA/D. The computationally efficient FEA modeling method is indispensable for this optimization. The results of MOO are an archive of all evaluated designs, and an estimate of Pareto front is sketched in the 3D space and also projected to the 2D plane. Among those designs, three optimal designs are selected according to 3 different selection criteria. After an optimal design is found, it is shown that a local sensitivity analysis can be used to investigate the margin for improvement and examine the design's robustness.

The results of this optimization reveal significant potential for bearingless IMs to provide the same motor performance as high performance IMs while gaining the substantial benefit of magnetic levitation. Several candidate designs are found with an efficiency $> 95\%$ and a torque density in the range of high performance servo motors, all of which require less than 1% of the stator current to support the rotor's weight. Overall, this paper shows that a bearingless IM is a viable and compelling option for medium to high power industrial compressors provided that manufacturing challenges of the pole-specific rotor winding can be overcome.

REFERENCES

- [1] R. P. Jastrzebski, P. Jaatinen, H. Sugimoto, O. Pyrhnen, and A. Chiba, "Design of a bearingless 100 kw electric motor for high-speed applications," in *Electrical Machines and Systems (ICEMS), 2015 18th International Conference on*, Oct 2015, pp. 2008–2014.
- [2] R. P. Jastrzebski, P. Jaatinen, A. Chiba, and O. Pyrhnen, "Efficiency of buried permanent magnet type 5kw and 50kw high-speed bearingless motors with 4-pole motor windings and 2-pole suspension windings," in *The 15th International Symposium on Magnetic Bearings (ISMB15)*, Aug 2016, pp. 1–8.
- [3] R. P. Jastrzebski, P. Jaatinen, O. Pyrhönen, and A. Chiba, "Design of 6-slot inset pm bearingless motor for high-speed and higher than 100kw applications," in *Electric Machines and Drives Conference (IEMDC), 2017 IEEE International*. IEEE, 2017, pp. 1–6.
- [4] ——, "Design optimization of permanent magnet bearingless motor using differential evolution," in *2018 IEEE Energy Conversion Congress and Exposition (ECCE)*. IEEE, 2018, pp. 2327–2334.
- [5] Y. Fu, M. Takemoto, S. Ogasawara, and K. Orikawa, "Investigation of a high speed and high power density bearingless motor with neodymium bonded magnet," in *Electric Machines and Drives Conference (IEMDC), 2017 IEEE International*. IEEE, 2017, pp. 1–8.
- [6] Y. Kang and E. Severson, "Optimization framework for a large high speed bearingless permanent magnet motor," in *Sixteenth International Symposium on Magnetic Bearings*, 2018, pp. 1–10.
- [7] Y. Kang and E. L. Severson, "Optimal design of 50kw concentrated winding bearingless motor," in *IEEE Energy Conversion Congress and Exposition (ECCE), 2018*.
- [8] Y. Duan and D. M. Ionel, "A review of recent developments in electrical machine design optimization methods with a permanent-magnet synchronous motor benchmark study," *IEEE Transactions on Industry Applications*, vol. 49, no. 3, pp. 1268–1275, 2013.
- [9] A. Tenconi, S. Vaschetto, and A. Vigliani, "Electrical machines for high-speed applications: Design considerations and tradeoffs," *IEEE Transactions on Industrial Electronics*, vol. 61, no. 6, pp. 3022–3029, 2014.
- [10] A. Chiba and J. Asama, "Influence of rotor skew in induction type bearingless motor," *IEEE Transactions on Magnetics*, vol. 48, no. 11, pp. 4646–4649, 2012.
- [11] Y. Sun, J. Tang, and K. Shi, "Design of a bearingless outer rotor induction motor," *Energies*, vol. 10, no. 5, p. 705, 2017.
- [12] J. Chen and E. L. Severson, "Design and modeling of the bearingless induction motor," in *2019 IEEE International Electric Machines and Drives Conference (IEMDC)*, May 2019, pp. 1–7.
- [13] A. Chiba, T. Fukao, and M. A. Rahman, "Vibration suppression of a flexible shaft with a simplified bearingless induction motor drive," *IEEE Transactions on Industry Applications*, vol. 44, no. 3, pp. 745–752, May 2008.
- [14] V. F. Victor, J. Á. de Paiva, A. O. Salazar, and A. L. Maitelli, "Performance analysis of a neural flux observer for a bearingless induction machine with divided windings," in *2009 Brazilian Power Electronics Conference*. IEEE, 2009, pp. 498–504.
- [15] A. Sinervo and A. Arkkio, "Rotor radial position control and its effect on the total efficiency of a bearingless induction motor with a cage rotor," *Magnetics, IEEE Transactions on*, vol. 50, no. 4, pp. 1–9, April 2014.
- [16] J. Lu, Z. Yang, X. Sun, C. Bao, and X. Chen, "Direct levitation force control for a bearingless induction motor based on model prediction," *IEEE Access*, vol. 7, pp. 65 368–65 378, 2019.
- [17] T. Tera, Y. Yamauchi, A. Chiba, T. Fukao, and M. A. Rahman, "Performances of bearingless and sensorless induction motor drive based on mutual inductances and rotor displacements estimation," *IEEE Transactions on Industrial Electronics*, vol. 53, no. 1, pp. 187–194, Feb 2006.
- [18] A. Chiba and J. A. Santisteban, "A pwm harmonics elimination method in simultaneous estimation of magnetic field and displacements in bearingless induction motors," *IEEE Transactions on Industry Applications*, vol. 48, no. 1, pp. 124–131, Jan 2012.
- [19] T. Wang, J. Huang, B. Lin, M. Kang, J. Chen, and W. Kong, "Eccentricity detection of a six-phase induction motor with hfi," *IET Electric Power Applications*, 2019.
- [20] N. R. Hemenway, H. Gjeddal, and E. L. Severson, "Magnetic bearing technology for industrial bearingless motor systems," in *2019 IEEE Workshop on Electrical Machines Design, Control and Diagnosis (WEMDCD)*, 2019.
- [21] K. Campbell *et al.*, "High-speed induction motor with an integrated gearbox for propulsion," 2017.
- [22] C. Di, I. Petrov, and J. J. Pyrhönen, "Modeling and mitigation of rotor eddy-current losses in high-speed solid-rotor induction machines by a virtual permanent magnet harmonic machine," *IEEE Transactions on Magnetics*, vol. 54, no. 12, pp. 1–12, 2018.
- [23] N. Uzhevov, E. Kurvinen, J. Nerg, J. Pyrhönen, J. T. Sopanen, and S. Shirinskii, "Multidisciplinary design process of a 6-slot 2-pole high-speed permanent-magnet synchronous machine," *IEEE Transactions on Industrial Electronics*, vol. 63, no. 2, pp. 784–795, 2016.
- [24] R. Lateb, J. Enon, and L. Durantay, "High speed, high power electrical induction motor technologies for integrated compressors," in *Electrical Machines and Systems, 2009. ICEMS 2009. International Conference on*. IEEE, 2009, pp. 1–5.
- [25] A. Smirnov, N. Uzhevov, T. Sillanpää, J. Pyrhönen, and O. Pyrhönen, "High-speed electrical machine with active magnetic bearing system optimization," *IEEE Transactions on Industrial Electronics*, vol. 64, no. 12, pp. 9876–9885, 2017.
- [26] C. Di, I. Petrov, J. J. Pyrhönen, and X. Bao, "Unbalanced magnetic pull compensation with active magnetic bearings in a 2 mw high-speed induction machine by fem," *IEEE Transactions on Magnetics*, no. 99, pp. 1–13, 2018.
- [27] D. Gerada, A. Mebarki, N. L. Brown, C. Gerada, A. Cavagnino, and A. Boglietti, "High-speed electrical machines: Technologies, trends, and developments," *IEEE Transactions on Industrial Electronics*, vol. 61, no. 6, pp. 2946–2959, 2014.
- [28] A. Chiba and T. Fukao, "Optimal design of rotor circuits in induction type bearingless motors," *IEEE Transactions on Magnetics*, vol. 34, no. 4, pp. 2108–2110, 1998.
- [29] E. L. Severson, R. Nilssen, T. Undeland, and N. Mohan, "Design of dual purpose no-voltage combined windings for bearingless motors," *IEEE Transactions on Industry Applications*, vol. 53, no. 5, pp. 4368–4379, Sept 2017.
- [30] J. Pyrhönen, T. Jokinen, and V. Hrabovcová, *Design of rotating electrical machines*. Wiley. com, 2009.
- [31] D. Gerada, A. Mebarki, N. L. Brown, K. J. Bradley, and C. Gerada, "Design aspects of high-speed high-power-density laminated-rotor induction machines," *IEEE Transactions on Industrial Electronics*, vol. 58, no. 9, pp. 4039–4047, 2011.
- [32] A. Chiba, T. Fukao, O. Ichikawa, M. Oshima, M. Takemoto, and D. Dorrell, *Magnetic Bearings and Bearingless Drives*. Newnes, 2005.
- [33] E. Severson, S. Gandikota, and N. Mohan, "Practical implementation of dual-purpose no-voltage drives for bearingless motors," *IEEE Transactions on Industry Applications*, vol. 52, no. 2, pp. 1509–1518, March 2016.
- [34] E. L. Severson, "Bearingless motor technology for industrial and transportation applications," in *2018 IEEE Transportation Electrification Conference and Expo (ITEC)*, June 2018, pp. 266–273.
- [35] M. T. Caprio, V. Lelos, and J. D. Herbst, "Design and stress analysis of a high speed rotor for an advanced induction motor," *CEM Publications*, 2004.
- [36] D. Meeker, "Finite element method magnetics," *FEMM*, 2010.
- [37] G. Y. Sizov, P. Zhang, D. M. Ionel, N. A. Demerdash, and M. Rosu, "Automated multi-objective design optimization of pm ac machines using computationally efficient fea and differential evolution," *IEEE Transactions on Industry Applications*, vol. 49, no. 5, pp. 2086–2096, 2013.
- [38] Q. Zhang and H. Li, "Moea/d: A multiobjective evolutionary algorithm based on decomposition," *IEEE Transactions on evolutionary computation*, vol. 11, no. 6, pp. 712–731, 2007.
- [39] R. Tanabe and H. Ishibuchi, "An analysis of control parameters of moea/d under two different optimization scenarios," *Applied Soft Computing*, vol. 70, pp. 22–40, 2018.
- [40] F. Biscani and D. Izzo, "esa/pagmo2: pagmo 2.10," Jan. 2019. [Online]. Available: <https://doi.org/10.5281/zenodo.2529931>
- [41] J. R. Hendershot and T. J. E. Miller, *Design of brushless permanent-magnet machines*. Motor Design Books, 2010.
- [42] P. Jaatinen, R. P. Jastrzebski, O. Pyrhönen, and A. Chiba, "Improving of bearingless 6-slot ipm motor radial force characteristics using rotor skew," in *2017 IEEE International Electric Machines and Drives Conference (IEMDC)*. IEEE, 2017, pp. 1–7.
- [43] G. Bramerdorfer, "Tolerance analysis for electric machine design optimization: Classification, modeling and evaluation, and example," *IEEE Transactions on Magnetics*, 2019.